small NANO MICRO

DOI: 10.1002/smll.200800439

Polarization Dependence of the C 1s X-ray Absorption Spectra of Individual Multi-Walled Carbon Nanotubes

Ebrahim Najafi, Daniel Hernández Cruz, Martin Obst, Adam P. Hitchcock, Bastien Douhard, Jean-Jacques Pireaux, and Alexandre Felten*

***T**he polarization dependence (linear dichroism) of the C 1s X-ray absorption spectrum of individual multi-walled carbon nanotubes (MWCNTs) is measured using scanning transmission X-ray microscopy. A very strong dichroic effect is found in the C 1s → π* transition, with almost complete disappearance of this transition when the electric-field (E)-vector is aligned parallel to high-quality (low-defect) MWCNTs and maximum intensity when the E-vector is orthogonal to the tube axis. In contrast, there is very little dichroism in the C 1s → σ* transitions. The origin of this polarization effect is explained. The magnitude of the polarization dependence is found to differ in MWCNTs synthesized by different methods (arc discharge versus chemical vapor deposition). This is ascribed to differences in densities of sp^2-type defects. The potential for use of this signal to characterize defects in single-carbon-nanotube devices is discussed.*

Keywords:
- carbon nanotubes
- linear dichroism
- scanning transmission X-ray microscopy
- sp^2 defects
- X-ray absorption spectroscopy

1. Introduction

Carbon nanotubes (CNTs) are often regarded as the building blocks of nanotechnology. Due to their exceptional properties CNTs are candidates for many engineering applications, such as electronic devices, field emitters, and gas sensors.[1–3] The potential of perfect CNTs is widely accepted. However, in most cases the actual materials are far from perfect, and so to realize such applications it is important to be able to monitor their electronic and mechanical character. The electronic, chemical, and mechanical properties of CNTs are correlated with their structure. From one sample to another, the composition of the powder and structure of the nanotubes can vary significantly. This is one of the most important challenges for advancing CNT-based nanotechnologies.[4] Electronic applications require nanotubes without chemical impurities or structural defects, since these cause electron scattering, which reduces electron mobility.[5,6] In other applications, certain types of defects are desirable since they can be used to control resistance,[6] to act as chemically specific sensors,[7] or as reactive sites for functionalization.[8] Thus, depending on the application, defective nanotubes may be either desirable or undesirable.

Conventional spectroscopy techniques such as near-edge X-ray-absorption fine-structure spectroscopy (NEXAFS)[9] and photoelectron spectroscopy (PES) are often used to study the electronic structure of CNTs. These techniques sample a large area and, therefore, the information obtained is an average property of the batch. Spectromicroscopy techniques, on the other hand, measure with high spatial resolution, thus allowing study of individual nanostructures. Kuzuo et al.[10] used electron-energy-loss spectroscopy (EELS) in transmission electron microscopy (TEM) to confirm the covalent character of the bonding across bundles of single-walled CNTs (SWCNTs) and multi-walled CNTs (MWCNTs). They reported two intense peaks for both SWCNTs and MWCNTs in the carbon edge region corresponding to the C 1s → π* and C 1s → σ* transitions, with those of the SWCNTs broader than those of the MWCNTs. Kuzuo et al. attributed this to the strong curvature of SWCNTs.[10] Stephan et al.[11] examined isolated SWCNTs and MWCNTs by TEM-EELS and showed that the spectral broadening was due to the presence of amorphous carbon impurities rather than tube curvature.

[*] Prof. A. P. Hitchcock, E. Najafi, Dr. D. H. Cruz, Dr. M. Obst
Brockhouse Institute for Materials Research
McMaster University
Hamilton, ON L8S 4M1 (Canada)
E-mail: aph@mcmaster.ca
B. Douhard, Prof. J.-J. Pireaux, Dr. A. Felten
LISE, University of Namur
61 rue de Bruxelles, Namur 5000 (Belgium)

Further, they investigated spectral variations across an isolated MWCNT and found differences between the spectra of the edges and center of the tubes, which they attributed to q-dependent scattering,[12] an effect analogous to linear dichroism in X-ray photoabsorption.[9] Recently, Saitoh et al.[13] employed an energy-filtered TEM-EELS system to study angular distributions of inelastically scattered electrons following core electron ionization of a MWCNT. They related the observed anisotropic angular distributions to the symmetry of the π^* and σ^* final states.

Previously, C 1s NEXAFS spectroscopy of CNT powders, films, and "forests"[14–16] has been used to characterize the degree of order and quality of CNT samples, typically correlating the intensity of the C $1s \rightarrow \pi^*$ transition with the fraction of sp^2 carbon sites. A detailed explanation of the expected systematic variation of the intensities of the C $1s \rightarrow \pi^*$ and C $1s \rightarrow \sigma^*$ peaks in an individual CNT as a function of the X-ray incident angle (i.e., the dichroic effect) has been given[15,16] but the predicted effect was not demonstrated experimentally since previous nonspatially resolved studies integrated over many CNTs that had different spatial orientations. To the best of our knowledge, this is the first experimental measurement of this effect in individual MWCNTs. Our results fully validate the published theoretical treatment of the linear dichroism of the C 1s spectra of CNTs.[15,16]

Scanning transmission X-ray microscopy (STXM) is a synchrotron-based microprobe technique that combines NEXAFS spectroscopy and microscopy with a spatial resolution currently routinely better than 30 nm.[17–20] We previously demonstrated the power of STXM to study isolated MWCNTs and to differentiate between the CNTs and various types of carbon impurities.[21,22] Although TEM-EELS provides much higher spatial resolution, it causes more radiation damage per unit analytical information than X-ray microscopy,[23] it has a significantly lower energy resolution than that of synchrotron-based spectromicroscopy, and measurement of linear dichroism via the momentum-transfer directional dependence is much less convenient than linear dichroism measurements with synchrotron X-ray sources.

This work reports the use of STXM to study the polarization dependence (linear dichroism) of the C 1s spectrum of individual CNTs. MWCNTs produced by arc discharge (AD) and chemical vapor deposition (CVD) are examined. The quantitative polarization dependence of the C $1s \rightarrow \pi^*$ transition is measured and shown to fit the function $C+A\cos^2(\theta)$, where A and C are constants and θ is the angle between the electric-field (E)-vector and the long axis of the CNT. This study provides the first measurement of NEXAFS dichroism of CNTs and shows that STXM has the potential to quantitatively probe defects in individual tubes.

2. Results and Discussion

2.1. Polarization-Dependent Spectroscopy

Figure 1 displays TEM (a, c, and d) and STXM (b and e) images of two different AD MWCNTs, one oriented approximately horizontally and the other approximately vertically. A higher resolution TEM image (Figure 1c) shows that the horizontal tube is actually composed of three tubes; one large one of 44 nm diameter, and two smaller ones of 16 and 21 nm. Figure 1f plots the C 1s spectra of parts of each tube. The dotted lines on Figure 1b and e identify the sub-regions from which these spectra were extracted. In order to remove the effect of the differences in thickness and number of layers of the two different tubes, the intensity scale of each spectrum was set by matching the intensity above 320 eV to that for 1 nm of elemental carbon at a density of 2.2 g cm^{-3} (that of graphite). Since the size and shape of each MWCNT are well characterized by TEM, it is possible to use the intensity of the measured spectrum along with the optical response of carbon, as reported in a standard database for X-ray constants,[24] to estimate the density for each MWCNT. The density for the vertical tube is estimated to be 0.60 g cm^{-3} from the ratio of the observed OD to that predicted for carbon of the known size, assuming unit density. In the same way, the density for the

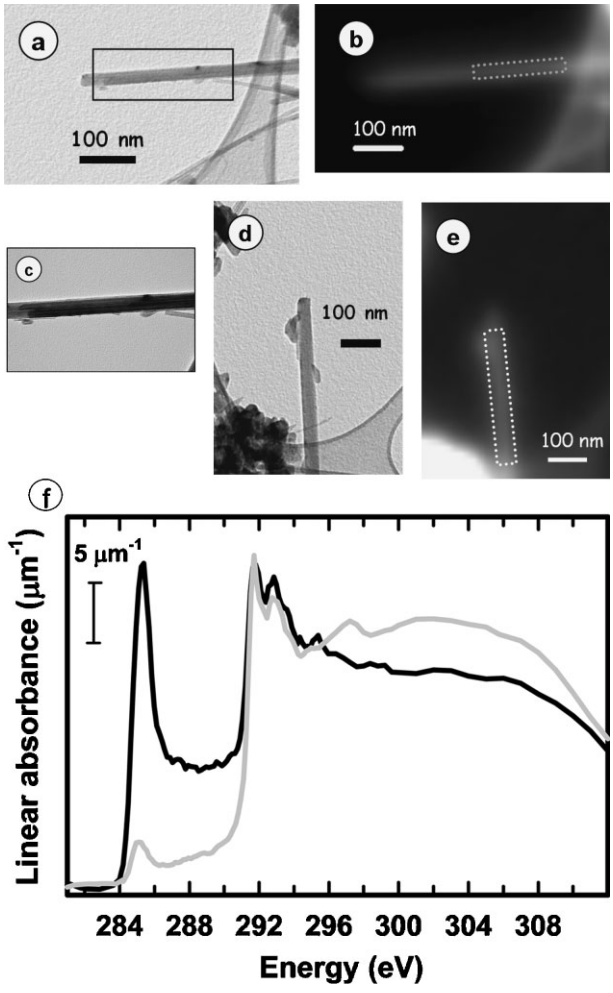

Figure 1. a, c, and d) TEM and b, and e) STXM images of two AD-MWCNTs. c) An expansion of (a), showing that it consists of two parallel MWCNTs enclosed in a third nanotube. f) C 1s spectra of these two nanotubes recorded with linear horizontally polarized light ([82 ± 5]%) using the STXM at beamline 5.3.2 at the Advanced Light Source (ALS). The gray curve corresponds to the spectrum of the tube oriented approximately horizontally (b), while the black curve corresponds to the tube oriented approximately vertically (e). In each case the spectrum is that of the region indicated by the dotted gray rectangles (ALS).

small NANO MICRO

assembly of three horizontal tubes is estimated to be 0.80 g cm^{-3}. This approach assumes that i) the MWCNT is approximated as a solid structure (i.e., ignoring the likely presence of a large hole at the center); ii) STXM has a spatial resolution such that the spectral signal only comes from the MWCNT and not the adjacent region of empty space. In fact, both of these approximations are invalid, so the density is clearly underestimated.

While some details are different, the polarization-dependent C 1s spectra displayed in Figure 1f are similar to those of highly oriented pyrolitic graphite (HOPG).[15,25] There is a sharp 1s → π* transition at 285.1 eV, a sharp 1s → σ* excitonic transition at 291.5 eV, and a broad 1s → σ* band peaking at 292.8 eV. This is followed by broad transitions of mixed symmetry peaking at 297 and 304 eV. These same features are observed in literature NEXAFS spectra of CNTs.[15,16] The main π* (285.1 eV) and broad σ* (292.8 eV) bands are seen in TEM-EELS spectra but the sharp excitonic transition at 291.5 eV is not present in TEM-EELS spectra, probably because of energy-resolution limitations. Although there is a broad intensity plateau between 287 and 290 eV, corresponding to an extended π* band, the spectra of the arc discharged MWCNTs do not exhibit sharp features in this range, where C 1s → $\pi^*_{C=O}$ transitions of oxygenated moieties occur,[22,23,26] indicating that the AD-MWCNT tubes were not significantly oxidized.

While the transition energies for both orientations are identical, the transition intensities differ dramatically. In particular, the C 1s → π* transition is very weak in the horizontal orientation, whereas it is the strongest transition in the vertical orientation. The σ* exciton (291.5 eV) has the same intensity for the two orientations, while the C 1s → σ* band (292.8 eV) is slightly weaker for the horizontal than for the vertical MWCNT. This is consistent with the observations of Banerjee et al.[15] who also observed little variation in intensity of the σ* resonances with changes in experimental geometry (in their case, changes in the angle of photon incidence). Other studies have shown that there is significant symmetry mixing of higher energy σ* and σ*+π* orbitals of HOPG,[25] which is further enhanced in nanotubes due to curvature-induced rehybridization effects. This mixing probably explains why the exciton peak at 291.5 eV is less prominent in MWCNTs than in HOPG. For orientation analysis of nanotubes, it is more informative to focus on the C 1s → π* peak, and the remainder of this paper deals only with the dichroic aspects of this feature.

2.2. A Simple Model for the Polarization Dependence

The following is a simple model for the linear dichroism of the C 1s spectrum of an isolated CNT. A similar analysis has been presented in greater detail elsewhere.[15]

The intensity of an inner shell excitation transition is determined by the matrix element $|\langle f|\underline{E}\cdot\underline{r}|i\rangle|^2$, where f and i are the final and initial states of the transition, $\underline{E}$ is the E-vector of the light, and $\underline{r}$ is a position vector. This equation can be reduced to $A\cos^2\theta$, where θ is the angle between $\underline{E}$ and a reference direction (which in this work is taken to be the long axis of the CNT) and $\underline{A}$ is a constant.[9] As with other highly anisotropic materials where the electronic states adopt specific spatial orientations, an angular dependence of the electronic-excitation intensity is expected. The local structure of a CNT can be regarded as approximately the same as that of graphene.[27] In graphene, when the E-vector is normal to the surface, only C 1s → π* transitions are allowed, whereas when the E-vector is parallel to the surface, only C 1s → σ* transitions are allowed. The situation is considerably modified in CNTs since rolling the graphene sheet breaks down this simple picture.

Figure 2a and b shows cartoons of a section of nanotube in both horizontal and vertical orientations. We consider the allowed or forbidden character of 1s → π* transitions with a fixed, horizontal E-vector and four situations: i) top/bottom and ii) sides of a horizontal nanotube, and iii) top/bottom and iv) sides of a vertical nanotube. Table 1 summarizes the expected allowed or forbidden character for these four situations which are depicted in Figure 2a and b. When the E-vector is aligned along the tube ($E_{//}$), 1s → π* transitions are forbidden at both carbon sites (A_1, B_1) whereas all of the 1s → σ* transitions are allowed. When the E-vector is orthogonal to the tube ($E_\perp$), 1s → π* transitions are only allowed at carbon atoms on the sides of the tube (B_1), while

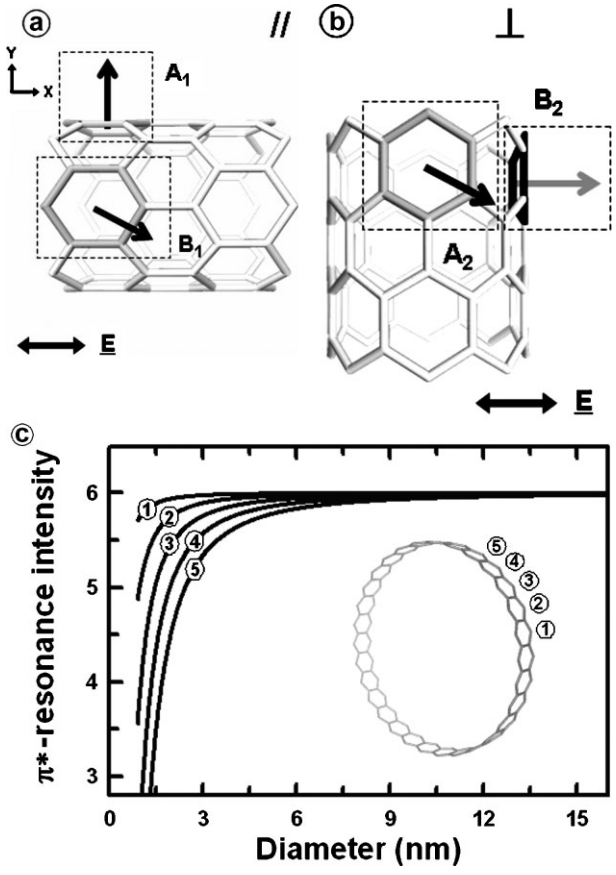

Figure 2. Cartoon explaining origin of the polarization effect. E-vector is fixed horizontally. a) The long axis of the nanotube is parallel to E. b) The long axis of the nanotube is perpendicular to E. A_1, B_1, A_2, and B_2 are transition moment vectors for C 1s → π* transitions in the selected rings (indicated by dashed rectangles; B_1 and A_2 transitions are out of the plane of the figure. c) Variation of the π* transition intensity as a function of the nanotube diameter, calculated for the rings number-coded in the inset image. The E-vector is perpendicular to the tube axis.

Table 1. Qualitative explanation of polarization dependence of the C 1s spectral features of large CNTs treated as rectangular tubes of graphene sheets.

Orientation[a]	Transition	Site[b]	Status
Parallel (see Figure 2a)	C 1s → π*	A_1	Forbidden
		B_1	Forbidden
	C 1s → σ*	A_1	**Allowed**
		B_1	**Allowed**
Perpendicular (see Figure 2b)	C 1s → π*	A_2	Forbidden
		B_2	**Allowed**
	C 1s → σ*	A_2	**Allowed**
		B_2	Forbidden

[a] Orientation of the long axis of the CNT relative to the E-vector.
[b] See Figure 2 for identification of these sites.

$1s \rightarrow \sigma^*$ transitions are allowed only at carbon atoms at the top/bottom of the tube (A_1). Within this simple model, the intensity of the π* transition is either on ($E_\perp$) or off ($E_{//}$) while the intensity of the σ* features only changes partially. Thus, one expects the largest linear dichroism in the C $1s \rightarrow \pi^*$ transitions, as is observed. This perspective is valid when the diameter of the tube is sufficiently large so that each side of the tube behaves like a graphene sheet. As the diameter of the nanotube decreases, each ring contributes partially to the in-plane and out-of-plane transitions. For a zigzag SWCNT and $\underline{E}$ normal to the tube, π* intensities in six-membered carbon rings are given by $I_{\pi^*}(i) = 6\cos^2(2\pi\phi_i)/N)$ where ϕ_i corresponds to the location of the ring and N is the total number of rings around the circumference. Figure 2c plots the predicted variation of the π*-resonance intensity as a function of the tube diameter, determined using this formula. At small diameters, the angle between the adjacent rings is large, leading to significant changes in the projected E-vector on adjacent rings. This is analogous to π–σ mixing in small-radius nanotubes.[10] As the diameter increases, this angle decreases such that, for tube diameters above ≈8 nm, the tube can be treated as a hollow rectangular box with graphene walls.

2.3. Polarization Dependence for AD-MWCNTs

It is well established that MWCNTs produced by AD methods are highly crystalline. In contrast, MWCNTs produced by CVD methods have much more defective structures. We have measured the polarization-dependent C 1s spectra of AD and CVD MWCNTs to show that these differences in defect concentrations result in differences in the linear dichroism measured from individual MWCNTs.

At the Canadian Light Source (CLS) spectromicroscopy beamline (10ID1) the beam is 100% linearly polarized and the polarization angle can be varied from −90 to +90°[28] by changing the relative positions of the girders in the elliptically polarized undulator (EPU). This makes it much easier to measure the intensity of the π* transition as a function of the angle between the axis of the MWCNT and the E-vector, and thus the detailed polarization results are taken from studies at the CLS STXM. Measurements of the full angular dependence were also made at the Advanced Light Source (ALS) using sample rotation. Those results (not shown) are in good agreement with the CLS results, when the incomplete linear polarization ($[82 \pm 5]\%$)[29] of the ALS bend magnet beamline is taken into account. The intensity of the C $1s \rightarrow \pi^*$ transition was measured as a function of polarization angle (varied by changing the EPU phase) by recording images at 283.0 eV (pre-edge) and 285.1 eV (π* peak), converting to optical density, and subtracting them from each other. The resulting difference is called a π* image.

Figure 3 shows π* images of an AD-MWCNT at various polarization angles in the −90° and +90° range. The tube axis was located at 30° relative to horizontal. Based on the expected polarization response, the C $1s \rightarrow \pi^*$ transition should have the lowest intensity when the E-vector is parallel to the tube (−30°) and the highest intensity when the E-vector is normal to the tube (+60°). The π* images shown in Figure 3 are consistent with these expectations. We also observed a polarization dependence for some portion of the carbon impurities located at the right-hand side of the image, indicating that such impurities are some type of crystalline form of graphite such as carbon onions. In contrast, other parts of the impurities such as the ''blob'' in the middle of the tube were not polarization sensitive, suggesting that such impurities are amorphous carbon.

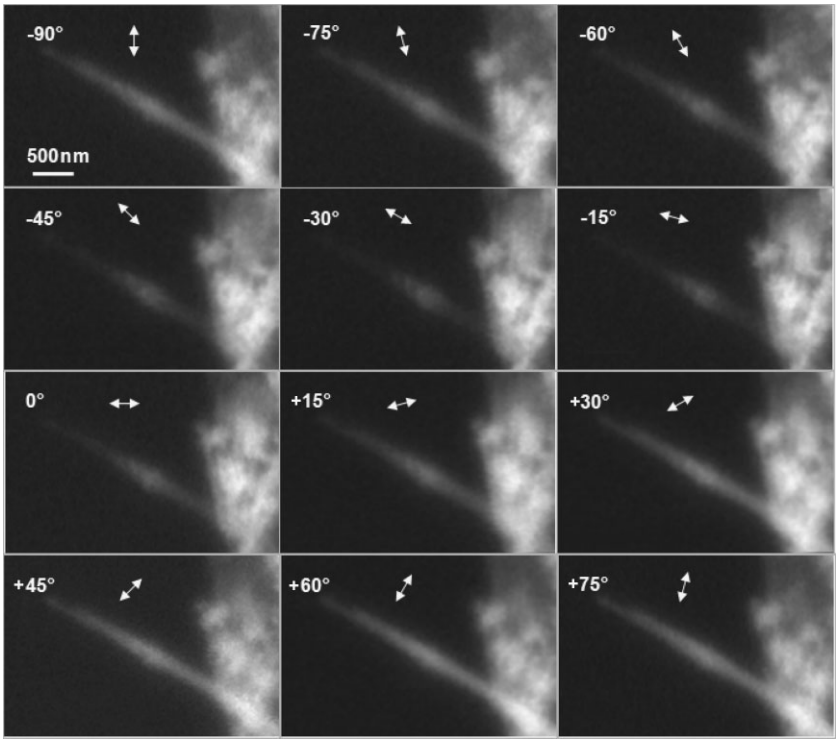

Figure 3. π* images (difference in optical density images at 285.1 and 283.0 eV) of an AD-MWCNT recorded with the indicated angles of the E-vector (0° is horizontal) (CLS).

small NANO MICRO

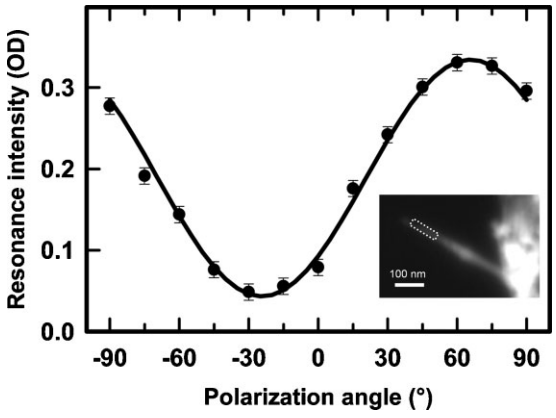

Figure 4. Polarization dependence of the C 1s → π* transition from the indicated region (gray outlined rectangle) of an AD-MWCNT (CLS).

The π* images obtained at various polarization angles were aligned and combined to form an angle-dependent image sequence. The angle-dependent intensity was then extracted from the region of the AD-MWCNT exhibiting the largest effect. Figure 4 plots this intensity as a function of the angle of the E-vector (horizontal = 0°, anticlockwise is positive). The inset shows the average of all the π* images, and identifies the subregion from which the signal was extracted. The minimum intensity was obtained at −30° and the maximum intensity was obtained at +60°. The experimental values were fit to $C + A\cos^2(\theta - \theta_{ref})$, where θ_{ref} is an optimizable parameter corresponding to the angle between the long axis of the MWCNT and the horizontal. There is good agreement between the fit (solid line) and the experimental data (Figure 4). Table 2 presents the results of the fit. The derived angle for the maximum signal was 65°, consistent with the spatial orientation of the MWCNT. Overall, the good agreement of the measured and predicted polarization dependence confirms that this signal is due to linear dichroism.

2.4. Polarization Dependence of CVD-MWCNTs

The polarization dependence of the C 1s → π* intensity of a CVD-MWCNT sample was also measured in order to investigate the effect of structural defects on the polarization signal. Figure 5 shows π* images of a CVD-MWCNT sample, recorded at various polarization angles over a range of −60 to +90°. Some regions are oriented horizontally while others are inclined with a large vertical component, thus allowing a sampling of a range of dichroic responses.

Figure 6 plots the C 1s → π* intensities extracted from two sub-regions as a function of polarization angle. The inset in Figure 6 indicates the locations of these two sub-regions, one approximately horizontal and the other inclined at 56° relative to horizontal. The results confirm the visual observation (Figure 5) that the maximum (minimum) intensity occurs when the E-vector angle is at 90° (0°) for the horizontal region, represented by solid lines, and at 38° (−52°) for the selected inclined region, represented by dotted lines. The experimental values were fit as was done for the AD-MWCNT data. Table 2 presents the results of the fit. There is good agreement between the experimental values (points) and the fits (solid lines) (Figure 6). The derived reference angles were 86 ± 4° and 38 ± 4°, consistent with the observed orientations of the selected regions in the CVD-MWCNT.

Table 2. Parameters derived from analysis of the polarization dependence of C 1s → π* transition intensities in individual AD- and CVD-MWCNTs.

Sample—region	Observed angle[a]	θ_{ref}	C	A
AD—dashed lines	30	65 ± 4	0.05 ± 0.01	0.27 ± 0.01
CVD—solid lines	0	86 ± 4	0.12 ± 0.01	0.22 ± 0.01
CVD—dashed lines	56	38 ± 4	0.11 ± 0.01	0.24 ± 0.01

[a] Reference line for angle determination is horizontal (θ = 0°, clockwise is positive).

For a defect-free nanotube, the π*-resonance intensity is zero when E is parallel to the tube and maximum when it is perpendicular to the tube. Thus the $I_{\parallel}/I_{\perp}$ ratio can be used as a

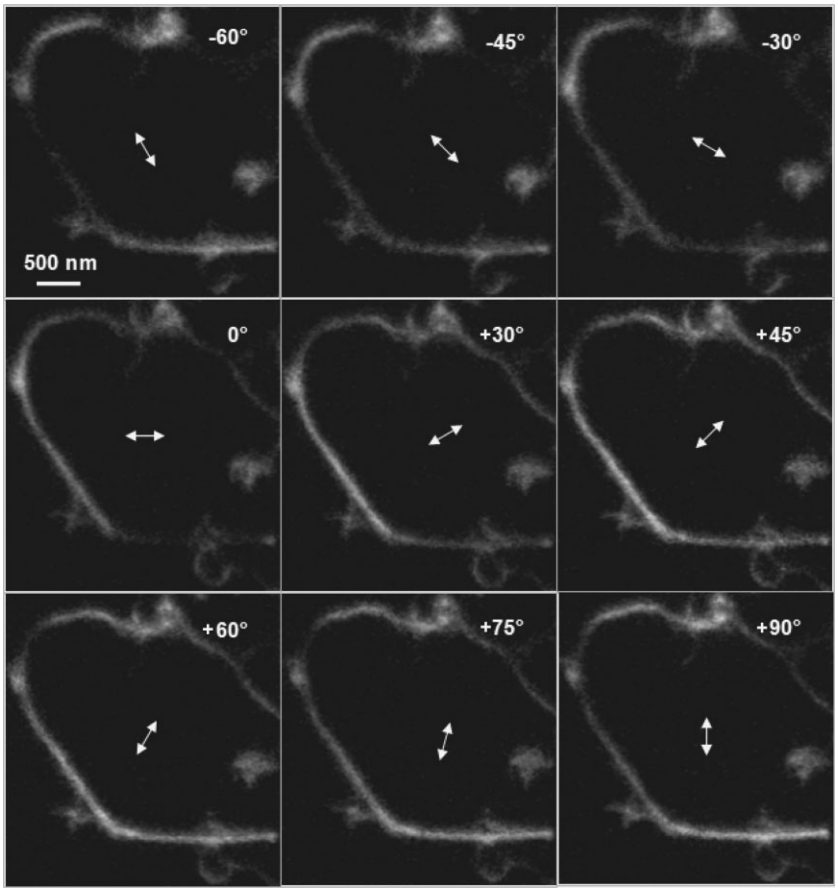

Figure 5. π* images of a CVD-MWCNT recorded with the indicated angles of the E-vector (0° is horizontal) (CLS).

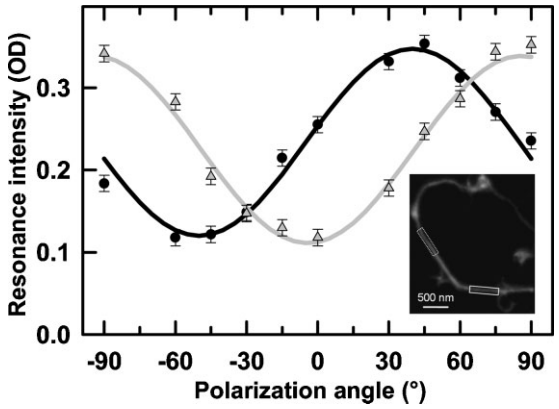

Figure 6. Polarization dependence of the intensity of the C 1s → π* transition from the indicated regions of a CVD-MWCNT (solid and dotted lines correspond to the gray and black curves, respectively) (CLS).

quantitative measure of the extent of non-sp^2 character (called sp^2 defects). Evaluating CNT quality with this ratio directly accounts for variations in thickness or density among a set of nanotubes. For the regions with their dichroism plotted in Figure 4 and 6, $I_{\parallel}/I_{\perp} = 0.15 \pm 0.03$ for the AD-MWCNT and $I_{\parallel}/I_{\perp} = 0.33 \pm 0.03$ for the CVD-MWCNT, indicating that the CVD nanotube is significantly more defective than the AD nanotube, as expected. Maps of the $I_{\parallel}/I_{\perp}$ ratio along individual CNTs provide a means of probing the spatial distributions of sp^2 defects. As the spatial resolution of STXM improves, or if similar dichroic signals can be measured with TEM-EELS, it will be possible to obtain detailed characterization of sp^2-defect density along individual nanotubes.

3. Conclusions

STXM applied to individual MWCNTs has shown for the first time that the C 1s → π* transition exhibits a strong linear dichroism with maximum intensity when the E-vector is perpendicular to the MWCNT axis. Using an STXM with an EPU capable of inclining the E-vector over a full 180° greatly facilitates characterization of dichroism. Comparison of AD- and CVD-MWCNTs showed that the π* dichroic magnitude correlates with the quality of the CNT, indicating that the dichroic effect can be used to map sp^2 defects along individual nanotubes and thus help optimize single CNT-based devices. We note that Sfeir et al.[30] recently demonstrated that the polarization dependence of Rayleigh and Raman scattering of visible laser light from individual CNTs can be used to characterize their quality. Relative to that approach, STXM constitutes a further advance, since it is able to probe small regions (≈25 nm) along individual CNTs.

4. Experimental Section

MWCNT powders were purchased from Mercorp (AD grown)[31] and NanoCS (produced by metal catalyzed CVD)[32] and used without modification. Nanotubes produced using these two methods were chosen because of their known structural differences. The AD method, which produces CNTs through vaporization of two opposing carbon rods in a chamber filled with an inert gas at high temperature, results in very crystalline nanotubes containing very few defects, but there are many side products such as graphitic onion particles, which are difficult to separate from the high quality AD-MWCNTs. The CVD method, which produces the tubes via vapor deposition of hydrocarbons on metal catalysts at relatively lower temperatures, results in higher purity, but the MWCNTs have much inferior mechanical and electronic properties due to the presence of many defects. Despite the lower quality, the CVD method is being aggressively pursued since it gives the possibility to grow CNTs on integrated circuits[33] or to align them on substrates.[34]

The AD-MWCNTs were dispersed in ethanol while the CVD-MWCNTs were sonically dispersed in dimethyl formamide. The solutions were drop cast onto a holey carbon TEM grid (AD) or onto a Si_3N_4 window (CVD). To remove residual solvent, the samples were heated overnight at 50 °C in the laboratory ambient. The AD-MWCNTs were previewed by TEM to pre-identify CNTs and to provide higher spatial resolution images for morphological characterization.[21,22]

Linear dichroism is an important aspect of NEXAFS of anisotropic samples. NEXAFS is electronic spectroscopy in which the excited state corresponds to events where an electron is excited from a core level to a level that is unoccupied in the ground state. Due to the short lifetime of the core excited state and the localized core hole the excitation occurs at a specific atom in a given structure. The excitation follows electric dipole selection rules, which means that excitation from a 1s core level is strongest to unoccupied levels in which there is a p-orbital lying along the E-vector. Here we focus on the 1s → π* transition which is only excited when the E-vector is oriented perpendicular to the surface of the CNT. A STXM[17–20] is used to measure NEXAFS of individual MWCNTs. In STXM a monochromated beam of X-rays is focused to ≈25 nm by a Fresnel zone plate, imaging at specific photon energies is performed by raster scanning the sample through the focal spot while measuring transmitted X-rays, spectral images are measured by recording images over a range of photon energies, and the linear dichroism is recorded by measuring multiple spectral images with the sample reoriented relative to a fixed linear polarization (ALS STXM532) or by using an EPU to rotate the E-vector in the plane of the fixed sample (CLS-STXM 10ID1).

The samples were measured using two different microscopes: the STXM on beamline 5.3.2 at the ALS[35,36] and the STXM on beamline 10ID1[37] at the CLS. At the ALS bend magnet beamline at the time of these measurements the X-rays were measured to be (82 ± 5)% linearly polarized.[29] At the CLS the X-rays are produced in an Apple-II type EPU, which produces essentially 100% linearly polarized light for which the spatial orientation of the E-vector can be adjusted over the range of −90 to +90° by changing the relative positions of the quadrants (phase) of the EPU.[28,38]

The MWCNT samples were measured using image sequences,[39] which were converted from transmission to optical density using the Io spectrum recorded simultaneously in the empty area around the MWCNT. After aligning the image sequence, spectra of the whole or a sub-region of an individual MWCNT were extracted.

NANO MICRO small

The polarization dependence of the C 1s → π* transition (285.1 eV) was then derived. For the ALS measurements, spectra were recorded from two separate MWCNTs oriented roughly perpendicular or parallel to the E-vector. For the CLS measurements, the polarization dependence of the same MWCNT was examined by using the EPU to rotate the orientation of the E-vector relative to the long axis of the MWCNT, and recording images at 283.0 eV (pre-C 1s onset) and 285.1 eV (π* peak). These images were then converted to optical density and subtracted from each other to obtain a single image corresponding uniquely to the π* signal.

Acknowledgements

This work was supported by NSERC, CFI, and Canada Research Chair, PAI 6 on "plasma surface interaction" (Belgium), the Nanobeams EU Network of Excellence and the EU-STREP project Nano2hybrids (no 033311). STXM measurements were carried out at beamline 5.3.2 at the Advanced Light Source (ALS) which is supported by the Office of Basic Energy Sciences of the US Department of Energy under contract DE-AC03-76SF00098. The Canadian Light Source (CLS) is supported by NSERC, CIHR, NRC and the University of Saskatchewan. We thank David Kilcoyne and Tolek Tyliszczak for their expert support of the ALS STXMs and Konstantine Kaznatcheev, Chithra Karunakaran and Drew Bertwistle for their support of the CLS STXM.

[1] H. W. Ch. Postma, T. Teepen, Z. Yao, M. Grifoni, C. Dekker, *Science* **2001**, *293*, 76.
[2] S. Fan, M. G. Chapline, N. R. Franklin, T. W. Tombler, A. M. Cassell, H. Dai, *Science* **1999**, *283*, 512.
[3] J. Kong, N. R. Franklin, C. Zhou, M. J. Chapline, S. Peng, K. Cho, H. Dai, *Science* **2000**, *287*, 622.
[4] N. Grobert, *Phys. Today* **2006**, *9*, 64.
[5] S. Frank, P. Poncharal, Z. L. Wang, W. A. de Heer, *Science* **1998**, *280*, 1744.
[6] C. Gómez-Navarro, P. J. De Pablo, J. Gómez-Herrero, B. Biel, F. J. Garcia-Vidal, A. Rubio, F. Flores, *Nat. Mater.* **2005**, *4*, 534.
[7] L. Valentini, F. Mercuri, I. Armentano, C. Cantalini, S. Picozzi, L. Lozzi, S. Santucci, A. Sgamellotti, J. M. Kenny, *Chem. Phys. Lett.* **2004**, *387*, 356.
[8] M. S. Raghuveer, A. Kumar, M. J. Frederick, G. P. Louie, P. G. Ganesan, G. Ramanath, *Adv. Mater.* **2006**, *18*, 547.
[9] J. Stöhr, *NEXAFS Spectroscopy*, Springer-Verlag, Berlin **1992**.
[10] R. Kuzuo, M. Terauchi, M. Tanaka, Y. Saito, *Jpn. J. Appl. Phys.* **1994**, *33*, 1316.
[11] O. Stephan, M. Kociak, L. Henrard, K. Suenaga, A. Gloter, M. Tencé, E. Sandré, C. Colliex, *J. Electron. Spectrosc. Relat. Phenom.* **2001**, *209*, 114.
[12] A. P. Hitchcock, T. Tyliszczak, *Surf. Rev. Lett.* **1995**, *2*, 43.
[13] K. Saitoh, K. Nagasaka, N. Tanaka, *J. Electron. Microsc.* **2006**, *55*, 281.
[14] Z. Li, L. Zhang, D. E. Resasco, B. S. Mun, F. G. Requejo, *Appl. Phys. Lett.* **2007**, *90*, 103115.
[15] S. Banerjee, T. Hemraj-Benny, S. Sambasivan, D. A. Fischer, J. A. Misewich, S. S. Wong, *J. Phys. Chem. B* **2005**, *109*, 8489.
[16] T. Hemraj-Benny, S. Banerjee, S. Sambasivan, M. Balasubramanian, D. A. Fischer, G. Eres, A. A. Puetzky, D. B. Geohegan, D. H. Lowndes, W. Han, J. A. Misewich, S. S. Wong, *Small* **2006**, *2*, 26.
[17] J. Kirz, C. Jacobsen, M. Q. Howells, *Rev. Biophys.* **1995**, *28*, 33.
[18] H. Ade, S. G. Urquhart, in *Chemical Applications of Synchrotron Rad*, Vol. *12A*, World Scientific, River Edge, NJ **2002**, p. 285.
[19] H. Ade, A. P. Hitchcock, *Polymer* **2008**, *49*, 643.
[20] A. P. Hitchcock, J. J. Dynes, G. A. Johansson, J. Wang, G. Botton, *Micron* **2008**, *39*, 741.
[21] A. Felten, H. Hody, C. Bittencourt, J. J. Pireaux, D. Hernandez-Cruz, A. P. Hitchcock, *Appl. Phys. Lett.* **2006**, *89*, 093123.
[22] A. Felten, C. Bittencourt, J. J. Pireaux, M. Reichelt, J. Mayer, D. Hernández-Cruz, A. P. Hitchcock, *Nano Lett.* **2007**, *7*, 2435.
[23] E. G. Rightor, A. P. Hitchcock, H. Ade, R. D. Leapman, S. G. Urquhart, A. P. Smith, G. Mitchell, D. Fischer, H. J. Shin, T. Warwick, *J. Phys. Chem. B* **1997**, *101*, 1950.
[24] a) B. L. Henke, E. M. Gullikson, J. C. Davis, *At. Data Nucl. Data Tables* **1993**, *54*, 181; b) X-ray Interactions with Matter. http://www-cxro.lbl.gov/opticalconstants/ (accessed January 2008).
[25] A. V. Sokolov, E. Z. Kurmaev, J. MacNaughton, A. Moewes, N. A. Skorikov, L. A. Finkelstein, *JETP Lett.* **2003**, *77*, 108.
[26] S. Banerjee, T. Hemraj-Benny, M. Balasubramanian, S. Sambasivan, D. A. Fischer, J. A. Misewich, S. S. Wong, *Chem. Phys. Chem.* **2004**, *5*, 1416.
[27] A. K. Geim, K. S. Novoselov, *Nat. Mater.* **2007**, *6*, 183.
[28] K. V. Kaznatcheev, Ch. Karunakaran, F. He, M. Sigrist, T. Summers, M. Obst, A. P. Hitchcock, *Nucl. Instrum. Methods Phys. Res., Sect. A* **2007**, *582*, 103.
[29] B. Watts, H. Ade, *J. Electron. Spectrosc. Relat. Phenom.* **2008**, *162*, 49.
[30] M. Y. Sfeir, F. Wang, L. Huang, C. C. Chuang, J. Hone, S. P. O'Brien, T. F. Heinz, L. E. Brus, *Science* **2004**, *306*, 1540.
[31] M. E. R. Corporation Homepage. http://www.mercorp.com/ (accessed January 2008).
[32] Nanocs Homepage. http://www.nanocs.com/ (accessed January 2008).
[33] R. G. Lacerda, A. S. Teh, M. H. Yang, K. B. K. Teo, N. L. Rupesinghe, S. H. Dalal, K. K. K. Koziol, D. Roy, G. A. Amaratunga, W. I. J. Milne, M. Chhowalla, D. G. Hasko, *Appl. Phys. Lett.* **2004**, *84*, 269.
[34] K. B. K. Teo, M. Chhowalla, G. A. J. Amaratunga, W. I. Milne, D. G. Hasko, G. Pirio, P. Legagneux, F. Wyczisk, D. Pribat, *Appl. Phys. Lett.* **2001**, *79*, 1534.
[35] A. L. D. Kilcoyne, T. Tyliszczak, W. F. Steele, S. Fakra, P. Hitchcock, K. Franck, E. K. Anderson, B. Harteneck, E. G. Rightor, G. Mitchell, A. P. Hitchcock, L. Yang, T. Warwick, H. Ade, *J. Synchrotron Radiat.* **2003**, *10*, 125.
[36] T. Warwick, H. Ade, A. L. D. Kilcoyne, M. Kritscher, T. Tyliszczak, S. Fakra, A. P. Hitchcock, P. Hitchcock, H. A. Padmore, *J. Synchrotron Radiat.* **2002**, *9*, 254.
[37] K. V. Kaznatcheev, Ch. Karunakaran, U. D. Lanke, S. G. Urquhart, M. Obst, A. P. Hitchcock, *Nucl. Instrum. Methods Phys. Res., Sect. A* **2007**, *582*, 96.
[38] A. T. Young, E. Arenholz, S. Marks, R. Schlueter, C. Steier, H. A. Padmore, A. P. Hitchcock, D. G. Castner, *J. Synchrotron Radiat.* **2002**, *9*, 270.
[39] C. Jacobsen, S. Wirick, G. Flynn, C. Zimba, *J. Microsc.* **2000**, *197*, 173.

Received: March 26, 2008
Revised: August 13, 2008
Published online: November 6, 2008

